ORIGINAL ARTICLE

Effects of tool shoulder geometry on mechanical properties and microstructure of friction-stir welded joints of AA5083-0 aluminium alloys

F. Ortega[1], W. Fernández[1], J. F. Santa[2] and J. Unfried-Silgado[3]

[1] Universidad Autónoma del Caribe. Grupo IMTEF. Cl 90 # 46-112, Barranquilla, Colombia
[2] Instituto Tecnológico Metropolitano – ITM. Grupo MATYER. Medellín, Colombia
[3] Universidad de Córdoba. Departamento de Ingeniería mecánica. Grupo ICT. 230002, Cra 6 No. 77- 305, Montería - Córdoba, Colombia

ABSTRACT – Shoulder geometry is an important geometrical feature of tool design in friction stir welding since it has a strong effect on heat generation and material flow. In this paper the effect of shoulder geometry of tool on mechanical properties, microstructure evolution, and thermal history of friction stir welded joints of AA5083-O aluminium alloy. Two different shoulder geometries of tool named concave and featured (concentric circles) were used, both with cylindrical threaded pin. A set of samples were fabricated using a milling machine and a factorial experimental design to estimate the effects of process parameters (rotational and welding speed) and shoulder geometry on welded joints. Tensile strength, hardness, and microstructure evolution were experimentally measured. These observations were complemented with results obtained from a finite element modelling to calculate thermal history in welded joints. The results showed that the combination of revolution pitch R-value and shoulder geometry of tool were the most significant factors, affecting to mechanical properties, thermal behaviour, and microstructure evolution. The best tensile properties were obtained with a featured shoulder tool using 1400 rpm and 16 mm.min^{-1}, and 1085 rpm and 11 mm.min^{-1} for rotational and welding speed. The same parameter combination resulted in a joint efficiency of 70% and 65%, respectively. In addition, the results of evaluation using an ANOVA analysis with fixed factors showed that increasing R-values produces statistically significant differences in ultimate strength (S_{ut}) values.

INTRODUCTION

Aluminium is the most popular non-ferrous metallic material in the world [1]. Aluminium alloys are widely used in structural fabrication, substituting other metals in aerospace, marine and automotive industries, owing to their high strength to weight ratio and formability, and availability in a wide variety of microstructural combinations and heat treatments [2–5]. Aluminium alloys of AA5xxx series are widely used in shipbuilding, naval construction (hulls and superstructures) and storage containers, because they exhibit a good combination of high tensile strength, excellent corrosion resistance, good weldability and conformability. Aluminium alloys of 5xxx series are essentially Al-Mg alloys, which are hardened by means of two concomitant mechanisms, solid solution and deformation [1, 2]. Mg contents in these aluminium alloys do not exceed 5% by weight. Mg atoms enter in solid solution in the lattice, allowing an appreciable increase of tensile strength (from 150 to 250 MPa), together with an acceptable maximum ductility close to 25% . Aluminium alloys AA5xxx series are commercially available in two conditions, hardened -H and annealed –O [2]. Alloys AA5083-O are used in fabrication of boats, cryogenic vessels, blades, compressor housings development, among other applications. The microstructure of those alloys consists of grains of γ-phase (matrix) in solid solution of Al-Mg, along with β-phase Al$_3$Mg$_2$, precipitating in grain boundaries, and possible presence of α-phase Al$_6$(Fe,Mn) precipitates. Alloys AA5083-O have a yield strength between 125 to 200 MPa, ultimate tensile strength (S_{ut}) between 275 to 350 MPa, and Vickers hardness between 75 to 90 HV [4].

Weldability of aluminium alloys AA5083 using conventional fusion welding process has been widely studied [6], [7]. The results of those studies showed that, even though, values of S_{ut} in AA5083-O welded joints using GMAW-P process present similar values to metal base, problems such as porosities and microcracks are still present [7]. Solid-state welding processes appear as an interesting alternative aiming to enhance weldability of this kind aluminium alloys [8]. Friction stir welding (FSW) is a solid-state joining process invented and patented in The Welding Institute (TWI) in 1991 [9]. In FSW process, problems related to state changes, such as, solidification, porosity, liquation cracking, and hot cracking are not undergone in welded metals joining [10, 11]. FSW is developed using a non-consumable rotating tool, which has two important parts: shoulder and pin, (see Figure 1). Welded joint in FSW is developed when a tool with a constant rotation speed (ω) is pushed down with an axial force (F_Z) and after welded joint is completed using a traverse speed (v_s) [12].
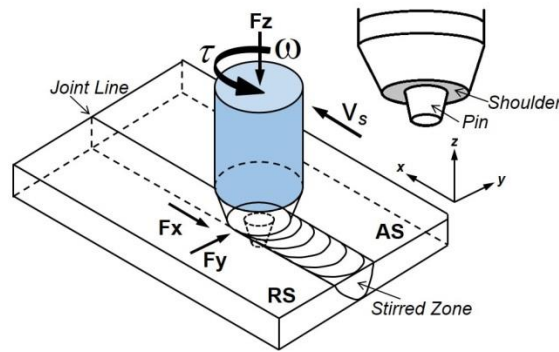
Figure 1. Schematic set of FSW shows parts and process parameters

Several studies have been developed aiming to understand weldability of AA5083 using FSW. Amini et al., [13] studied the effect of pin position in FSW on aluminium alloy AA5083-O. They observed that tool temperature increased when ω was increased. The authors concluded that tools with dislocated pin had more ability of mixing and forging material during welding and the samples also showed higher S_{ut}. Kumar et al., [14] developed a systematic study in FSW on AA5083-O using a factorial statistical model and experimental set aiming to understand the effects of parameters on heat input and process forces. They concluded that ω, v_s, and diameter of tool shoulder were the most significant parameters affecting F_Z and heat input. Jannet et al., [15] investigated by using a statistical optimization model the relationships between process parameters and optimal Sut in FSW of 6 mm thick of AA5083-O aluminium alloy. The authors found that values of ω of 1100 rpm and vs of 75 mm min^{-1} were the optimal parameters to obtain a maximum value of S_{ut}. Min-Su et al., [16] studied the incidence of process parameters (ω and v_s) on defects and mechanical properties of FSW welded joints of AA5083-O. The authors deduced that ω of 800 rpm and a v_s of 124 mm.min^{-1}, were the optimal parameters to maximize S_{ut}.

Taheri et al., [17] investigated the optimization of process parameters in FSW of AA5083 using radiography and ultrasonic non-destructive test (NDT) techniques. They modified ω and v_s values from 200 to 1000 rpm, and from 55 to 100 mm.min^{-1}, respectively. Results showed joints free of defects. However, there were formed lateral cavities due to insufficient heat input, caused by an incorrect ratio (R) ω/v_s. Imam et al., [18] welded by FSW thick plates (thickness ~20mm) of AA5083-O, and they observed that using a ω of 500 rpm and v_s of 50 mm.min^{-1}, a fully consolidated and defect free welded joint can be obtained. A uniform distribution of hardness caused by a fully annealed condition of base metal was also observed. Hirata et al., [19] studied the influence of process parameters of FSW in AA5083-O on its formability and final grain size. These authors found that in stir region a grain size refinement occurred because of increasing friction heat flow. The authors also found that hardness increased while a slight reduction in Sut and a ductility improvement was also observed. Klobcar et al., [20] studied the effect of FSW parameters on hardness and microstructure of a 4mm thickness plate of AA5083-O aluminium alloy. These authors observed that optimized properties and microstructure in FSW were developed using a revolution pitch or feed per revolution of 0.35 rev.mm^{-1}.

Finally, Thube [21] developed an investigation about the effect of pin tool profile on mechanical properties and microstructure in FSW of AA5083-O. This author concluded that welded joints fabricated using ω of 1400 rpm and cylindrical pin obtained Sut and defects-free welded regions. Fujii et al., [22] studied the effects of tool shape and process parameters on mechanical properties and microstructure of FSW in AA 5083-O. The authors evaluated three tool profiles and they found that the weldability is significantly affected by ω, obtaining a free-defects joint. Chen et al., [23] investigated the flow of material during FSW of 8 mm plate of aluminium alloy AA5083-O using a tool of AISI H13 steel. These authors observed formation of cavities in advanced side of welded joint, which probably is due to creation and detaching of a layer of material from the pin of tool on the trailing–retreating site during each revolution, which is continuously filled during process.

Some works have proved that heat generation in FSW is very sensible to geometry of tool together with process parameters, being tool shoulder the main responsible of frictional heat generation, Colligan and Mishra, and Schneider in [24, 25]. However, it is necessary to carry out more studies aiming to determine how is the influence of shoulder geometry on thermal distribution history, properties and microstructure in friction stir welded joints of AA5083-O, and their relationships. Accordingly, the aim of this work is to evaluate the effects of two different shoulder geometries of tool on mechanical properties, microstructure evolution, and thermal history of friction stir welded joints of AA5083-O aluminium alloy. The studied was carried out using a set of experimental tests and numerical modelling of the results.

METHODS AND MATERIALS

Materials

Plates of AA5083-O aluminium alloys with dimensions of 95 mm × 80 mm × 7.9 mm were used. Table 1 shows the chemical composition of plates, experimentally measured by optical emission spectrometry.

Table 1. Chemical composition of base metal (BM) and the tool material (TM) in weight-%

Item	Al	Si	Fe	Cu	Mn	Mg	Cr	Zn	Ti	Ni	V	Zr	Ca	C
BM	Bal.	0.088	0.253	0.008	0.7373	4.436	0.059	0.109	0.01	0.005	0.008	0.002	0.002	---
TM	---	1.10	Bal.	---	0.40	---	5.20	---	---	---	0.95	---	---	0.39

Table 2 summarizes the most important mechanical properties of plates, in the as-received condition before welding process. FSW tools were manufactured using an AISI H13 steel. The chemical composition of this steel is shown in Table 1 and the mechanical properties are shown in Table 3. After fabrication, tools were heat treated by preheating from room temperature to 500°C and heating at 1020°C. After that, oil quenching was performed and subsequently tempering at 280°C during 1h. Finally, plasma nitriding at 480°C during 10h was carried out, aiming to obtain a hardness of 55 HRC, high toughness, wear resistance and to avoid reheat microcracks.

Table 2. Properties of as-received AA5083-O base metal

Yield strength (MPa)	Ultimate tensile strength (MPa)	Hardness Vickers (HV)	Elongation (% in 50 mm)	Density (g.cm^{-3})
178.2 ± 5	331.8 ± 8	85 ± 1.5	25	2.67

Table 3. Mechanical properties of tool material

S_Y (MPa)	S_U (MPa)	Elongation (%)	Hardness HV
1650	1990	9.0	560

Process Parameters Selection

A monolithic tool with two different shoulder geometries was used. The dimensions, details and geometric characteristics are shown in Figure 2. The tool has a conical threaded pin and a shoulder diameter of 20 mm and a total length of 112.2 mm. Furthermore, the main dimensions of tool are the following: largest pin diameter 7.4 mm, pin height 7.2 mm, and the concave shoulder has a concavity angle of 6°. All welded joints were developed in flat position using butt joint configuration. Welding direction of FSW samples was selected perpendicularly to longitudinal direction of deformed metal base to keeping conventions.
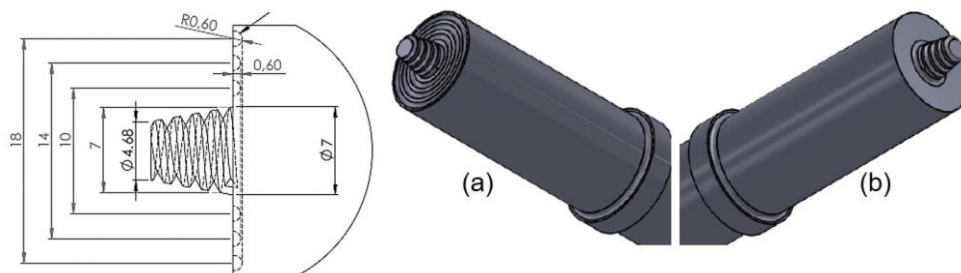

Figure 2. Dimensions and geometry of used tools. Details of shoulder geometry: (a) features with concentric circles and (b) concave

Welding tests were carried out using a universal milling machine FEXAC®, with 5 hp of nominal power. Process parameters selection was developed considering ranges of rotational and traverse speed combinations supplied by milling machine, including maximum value of torque 20 N.m. The process window was ranged from 11 to 500 mm.min^{-1}, and from 30 to 1400 rpm of traverse and rotational speeds, respectively, using 20 s of dwell time, in accordance to literature information [17–19].

A preliminary set of welded joints was carried out aiming to select best parameters for each kind of shoulder of tool. Welded joints were inspected using non-destructive techniques (visual inspection) and destructive techniques (metallographic observation). Criteria used to select the best process parameters were the following: presence of discontinuities (internal and external, especially pin-hole defect), excessive burr (> 5 mm), and incomplete penetration. Best combinations of process parameters for each tool were selected and replicated three times. This last set of welded joints was considered final tests.

Welded Sample Location

Specimens for hardness and tensile tests were extracted from positions of each welded plate from final testing set as is showed in Figure 3. Cuts were carried out using adequate cooling during operation aiming to avoid excessive heating. Specimens of tensile test were fabricated according to ASTM E8/E8M-09 standard. Tensile tests were developed using a Shimadzu® AGX test machine with a load cell of 100 kN, and a constant stroke speed of 5 mm.min^{-1} at room temperature. Microhardness tests were performed according to ASTM E384-09 standard using an Indenter ZTU® hardness machine with 100 g of load and dwell time of 10 s. Scanning of microhardness was carried out along of 50 mm to transversal section of each welded specimen leaving 2.5 mm between indentations.
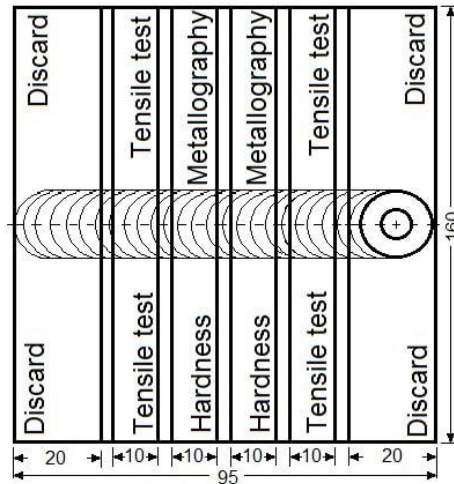

Figure 3. Sketch of welding coupon shows locations and geometry of samples

Microstructure Characterization

Metallographic observations were developed using optical and scanning electron microscopy. Specimens of microstructure evolution exploration were mounted in cold resin (polyester) with the aim of avoid heating that could alter the microstructure. All specimens were ground using sandpaper grades between 100 to 2000, followed by automated polishing using 0.3 μm alumina suspension. All polished specimens were etched with Keller's reagent (3 ml of HCl, 5 ml HNO$_3$, 2 ml 0f HF, 190 ml of distilled H$_2$O) during 10 s. Macroscopic (2X to 5X) observation was developed using a Stereoscopic Nikon SMZ 1500. Optical microscopic observations were performed in microscopes Nikon® series Eclipse LV 100 and Olympus® EX51. Finally, scanning electron microscopy observations were carried out in a SEM Jeol® JSM-7100F using 15 a 25 keV, secondary (SE) and backscattering (BSE) electron modes. An Oxford XMAX® 20 EDS detector was coupled to the SEM to perform chemical microanalysis.

Experimental Set

An experiment based on 2^K factorial statistical design completely randomized was applied, aiming to establish the influence of revolution-pitch (R) (rotational and traverse speed ratio) and surface area for each type of shoulder geometry on mechanical properties (S_y and S_{ut}) of welded joints. Each factor was evaluated using two different levels. It was developed analysis of variance (ANOVA) with the aim to evaluate the influence of factors on response variables. Later, it was analyzed the influence of one factor (shoulder geometry) on response variables. Experiments were developed, replicating tests in three times and a reliability of 5% was obtained.

Computational Modeling

A numerical modeling was developed using a computational domain of 80 mm in length, 95 mm in width, and 7.9 mm in thickness aiming to obtain thermal history of welded joints. Simulated tool geometries had the same conditions described in section 2.2. Domain was divided in two regions: (i) moving region, and (ii) stationary region. Each one of regions is connected to each other by means a pair of interfaces. The mesh scheme at the domain is shown in Figure 4.
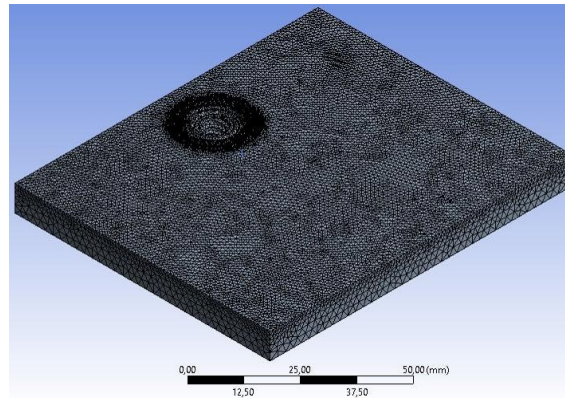
Figure 4. Image shows mesh of model domain

Tetrahedron geometry elements were used for the global characteristics of the mesh with a size of 1mm, with characteristic curve, fine smoothing and a growth rate of 1.2mm. It was made an independent mesh in the contact zone with the tool, using a treatment named body sizing®. This method overlaps a geometry size of 0.5mm for best results, and it was used on the threaded geometry inner faces and the edge that is in contact with the tool. Governing Eqs. of model are shown in Eqs. (1) to (4). Energy balance is presented in Eq. (1).

$$\frac{\partial}{\partial t}(\rho E) + \nabla \cdot \left(\vec{v}(\rho E + p) \right) = \nabla \cdot \left(k_{eff} \nabla T - \sum_j h_j \vec{J_j} + (\vec{\tau}_{eff} \cdot \vec{v}) \right) + S_h \tag{1}$$

Where, E is energy, ρ is density, v is velocity, T is temperature, p is pressure, k_{eff} is the effective conductivity coefficient, J_j is the diffusional flux of species. Eq. (2) shows the generated heat.

$$Q_g = 2\pi\omega\tau R^3 \left[\frac{1}{3} \left(\frac{R_H}{R} \right)^3 + \frac{H}{R} \right] \tag{2}$$

Where, Q_g is generated heat, ω is the angular velocity, H is the pin height, R_H is the shoulder radius, R is the pin radius, τ is the shear stress. For viscosity modelling was used the Carreau's model shows in Eq. (3)

$$\mu = \mu_\infty + \frac{(\mu_0 - \mu_\infty)}{(1 + (\lambda\dot{\gamma})^2)^{\frac{1-n}{2}}} \tag{3}$$

where μ_0 is the minimum value of viscosity, μ_∞ is the maximum value of viscosity, γ is the constant time, and n is the experimentally determined volumetric strain of material. All the parameters in the above equation are given in SI units. In this work, these values were adjusted to $\mu_0 = 0$, $\mu_\infty = 1.3 \times 10^{-7}$, $\gamma = 10$, and n = 0.25. The thermal conductivity k and specific heat C_p in function of temperature T are represented through Eqs. (3) and (4), according to Kim et al. [26].

$$C_p = 2.732 \times 10^{-11}T^5 - 7.602 \times 10^{-8}T^4 + 8.3166 \times 10^{-5}T^3 - 4.4683 \times 10^{-2}T^2 \\ + 1,2222 \times 10^1 T - 4.02 \times 10^2 \tag{4}$$

$$k = 1.3061 \times 10^{-11}T^5 - 3.4022 \times 10^{-8}T^4 + 3.4099 \times 10^{-5}T^3 - 1.6426 \times 10^{-2}T^2 + 3.9437T^{-2} \\ - 2.1394 \times 10^2 \tag{5}$$

A commercial software was used to solve the numerical modeling. Simulation was started with the regions at a temperature of 298K, tool with a rotational speed of 1400 rpm and a traverse speed of 16mm.min⁻¹. It was assumed that density of materials was constant, while thermal conductivity and heat capacity were temperature dependent. For the different parameters used in the boundary conditions, the inner faces were analyzed as rotational with a heat flow, the edge as stationary without heat flow and the other faces with a convection condition.

RESULTS AND DISCUSSION

Process Parameters Selection

Figure 5 shows the FSW process window for AA5083 aluminium alloy. Each filled circle represents two experimental data points corresponding to traverse and rotational speed extracted from literature. Red line represents linear fit of experimental data results from Joshi et al. [27], in which two regions of parameters combination are observed. At the top of Figure 5 a region with adequate heat inputs, which could produce defects-free welded joints in AA5083 alloys is located. Red rectangle (dotted lines) shows a region with a combination of process parameters delivered by milling machine used in this work. Heat input was determined using a preliminary set of welded joints. The preliminary parameters results are shown in Table 4.
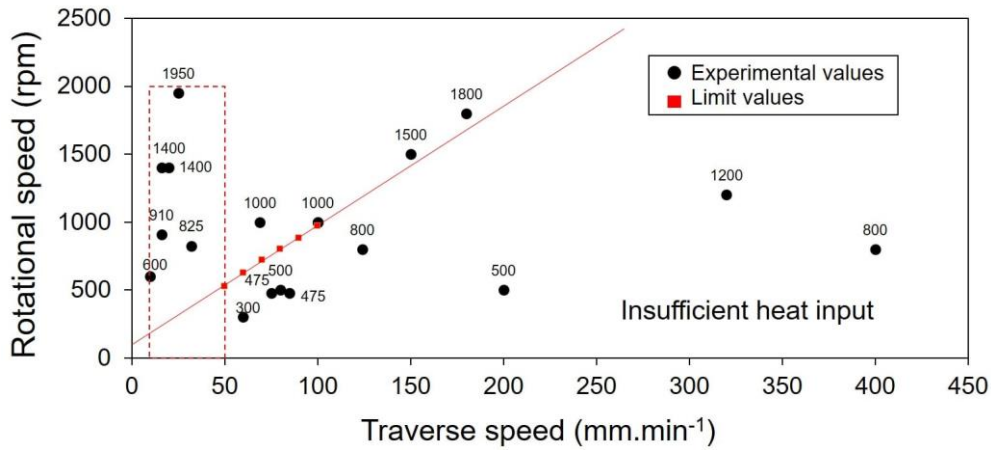
Figure 5. Process window for FSW in aluminium alloys AA5083

Table 4. Parameter process of preliminary for welding samples

Traverse speed	v_S (mm.min^{-1})	11	23	45	100
Rotational speed	ω (rpm)	1400	1085	840	500

From the evaluation of process parameters showed in Table 4, it can be determined that the combinations of high rotational speeds with low values of transverse speed produce the best quality in welded joints. That result agrees with the process windows information displayed in Figure 5. When the transverse speed is low, the tool remains enough time to provide an adequate heat input during welding.

Meanwhile, high values of traverse speed stimulate tunnelling defects and lack of consolidation in weld, which is coherent with results found by Lombard et. Al. and Leal & Loureiro, in [28, 29]. Based on preliminary results, operational values of rotational speed of 1085 and 1400 rpm, and traverse speed of 11 to 16 mm min-1 were chosen aiming to evaluate a final set of welded joints. Welded joints are shown in Figure 6. The joints were obtained using selected process parameters showed in Table 5. The final welded joints exhibited moderate burrs, no tunnelling defects, no lack of fill, and they were free of surface defects.
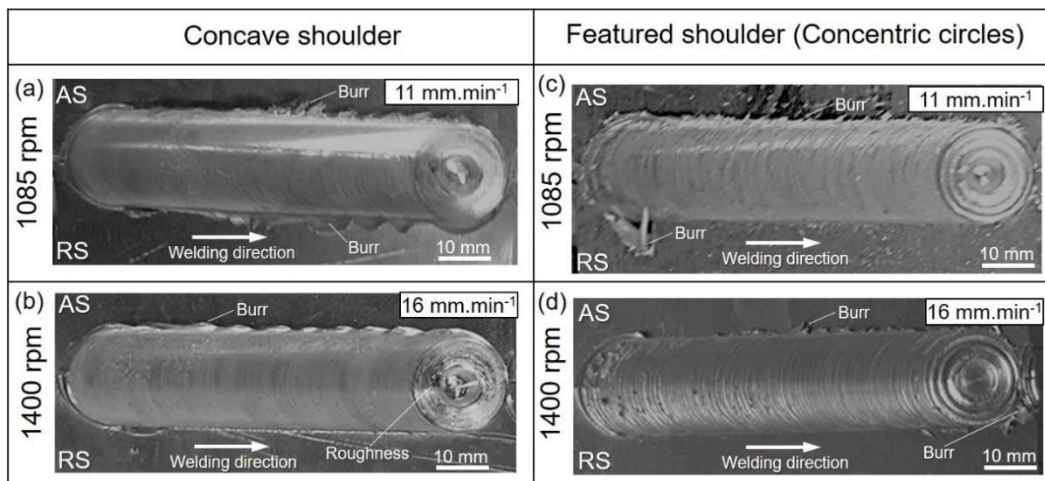

Figure 6. Images of final welded joints obtained with selected parameters and concave shoulder tool (a) and (b), and featured shoulder tool (c) and (d)

Table 5. Selected process parameters for final welded joints

Shoulder geometry	Concave		Featured	
Denomination	H – H	L – L	H – H	L – L
Rotational speed – ω (rpm)	1400	1085	1400	1085
Traverse speed – v_s (mm.min^{-1})	16	11	16	11
R [ω / v_s] (rev.mm^{-1})	87.5	98.6	87.5	98.6

Microstructure Evolution

Microstructure of base metal studied in this work exhibits anisotropic behaviour, as it is shown in Figure 7. Elongated grains of Al-rich γ-matrix are decorated with β-precipitates (Al_3Mg_2) along grain boundaries, and some sporadic precipitates of α-precipitates $Al_6(Fe,Mn)$ at intragranular positions (see Figure 8). Diffraction x-ray analysis of base metal (Figure 8d) before welding displays weak peaks of β (Al_2Mg_3), and α-$Al_6(Fe, Mn)$ second phases in an Al-rich γ-matrix, confirming low fraction of these intermediate phases, Choi et al, and Goswami et al, in [30, 31]. In the annealing condition, base metal presents low hardness and high ductility as it was shown in Table 2.

Figures 9 and 10 show the microstructure of the cross-section of all welded samples obtained using selected process parameters. For all combinations of process parameters and shoulder geometries of tool, a similar pattern of metal flow in stir region was obtained. Both, concave and featured shoulder produced the widest heat-affected zone when the parameters combination L-L was used.
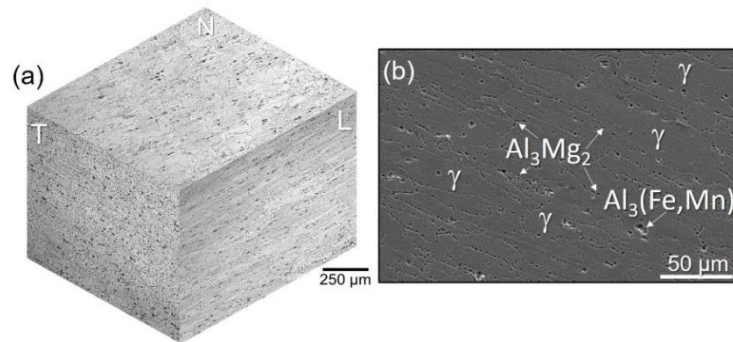

Figure 7. Optical microscopy arrangement image of metal base
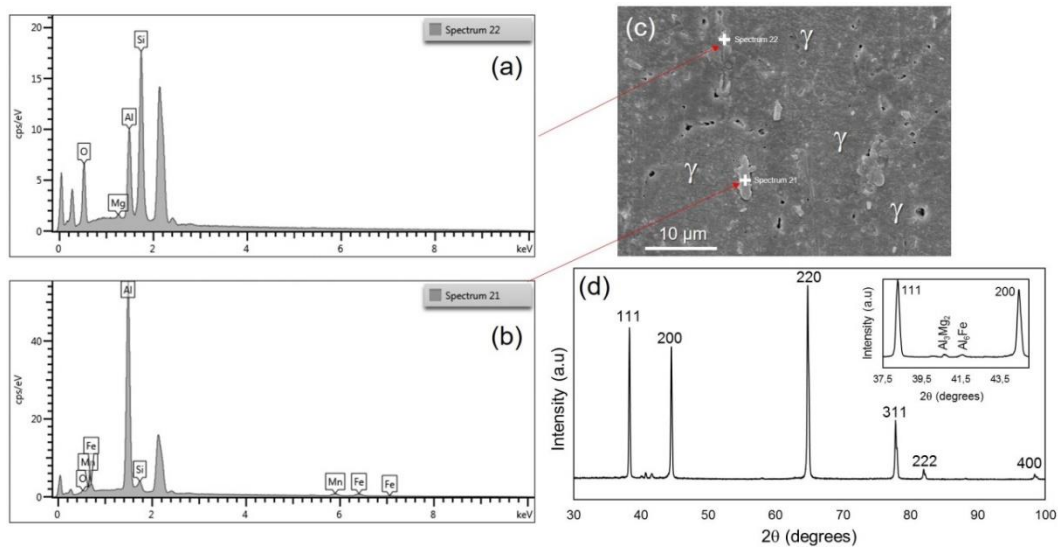

Figure 8. SEM-EDS images and analysis of chemical and morphology of precipitates (a) Al-Mg rich precipitate, (b) Al-Mn-Fe rich precipitate, (c) image region of analysis. (c) XRD pattern of base metal (compared with ICDD 00-004-0787 Card)

Details of the microstructure and local hardness at the stir region are displayed in Figure 11. There are two clearly distinguishable regions in stir zone (shoulder flow zone - SFZ in the top, and nugget zone - NZ in bottom), both produced by flow material pattern [23]. Some combinations between shoulder geometry and process parameters (L-L and L-H) produced adverse effects in stir region.

Cavities were observed in the interface SFZ / NZ, and they were more critical for higher R-values. Besides, when R-values increased, the hardness in stir zone also increased and its effect is more notorious for featured shoulder tools. These observations can be explained by the larger surface area in featured shoulder tools than concave shoulders, which favours plasticizer heat, Unfried et al., in [32]. The same combination of parameters that produced a wider HAZ (L-L) had higher hardness in the stir region.
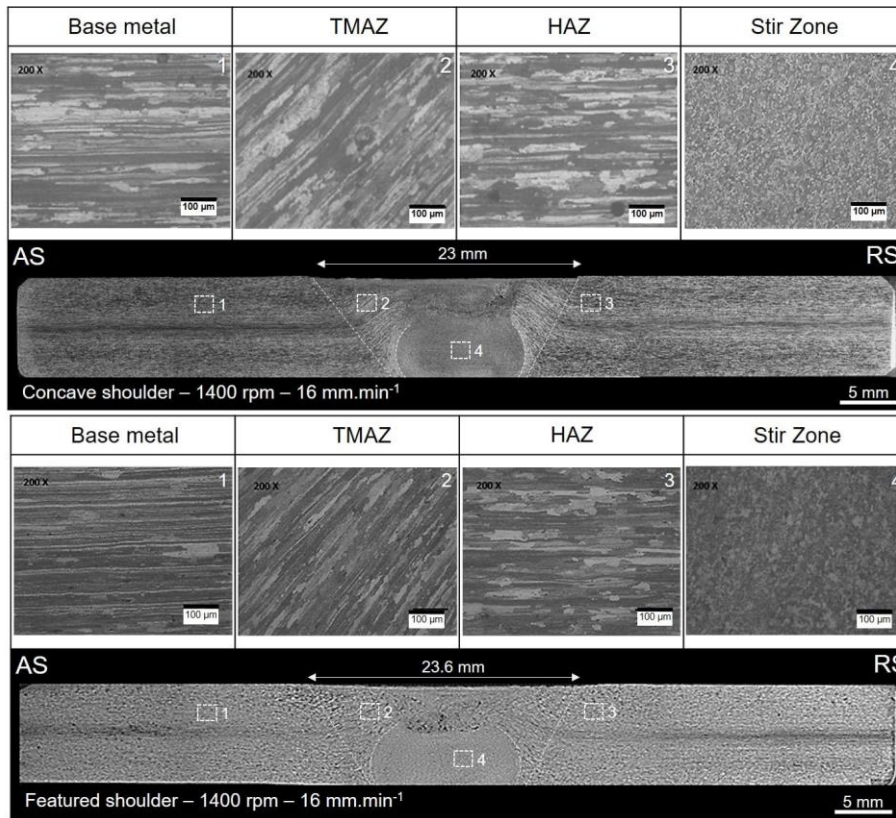
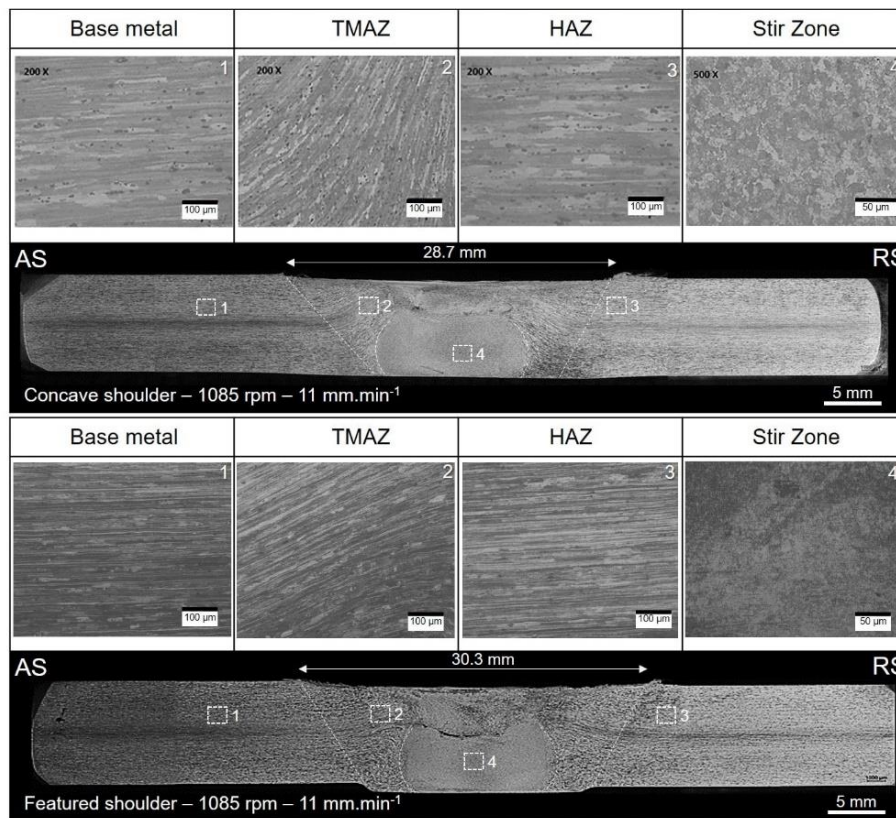**Figure 9.** Cross section of welded samples for parameters combination (H-H) 1400 rpm and 16mm.min^{-1}

Figure 10. Cross section of welded samples for parameters combination (L-L) 1085 rpm and 11mm.min^{-1}

Simulation of Thermal Evolution in Welded Joints

Results of thermal distribution at quasi-stationary stage for two different geometry shoulders and the H-H parameters combination are shown in Figure 12. It is possible to distinguish a different thermal distribution for each case. Featured shoulder tool concentrates heating near the tool pin at stir zone, where is obtained the highest peak of temperature. On the other hand, thermal distribution obtained using concave shoulder shows an extended region of heating around the stir zone. These results are consistent with hardness values measured in stir region observed during microstructure evolution characterization and found in others works [14–16].
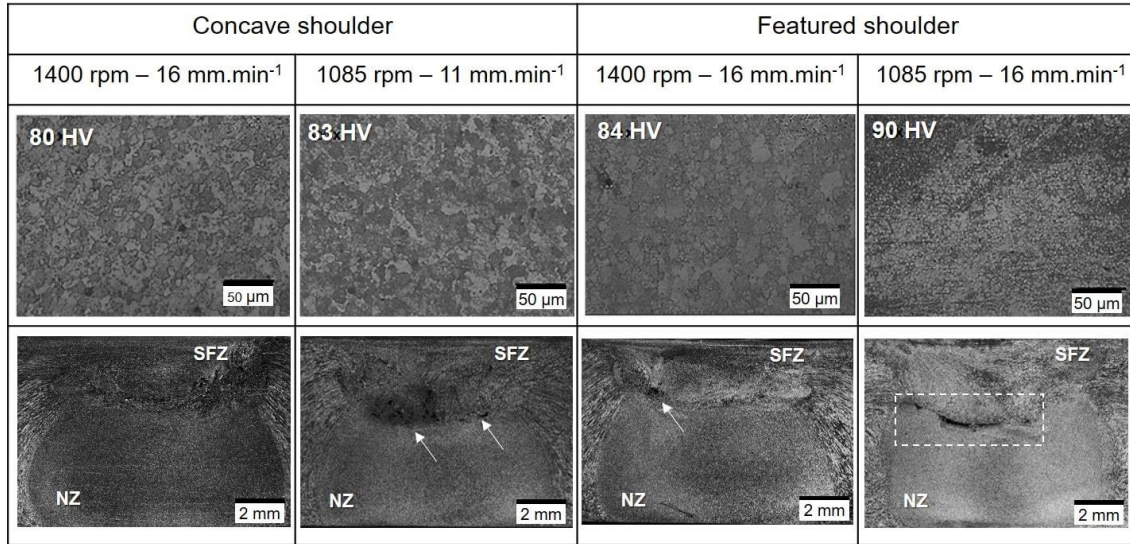

Figure 11. Microstructure of stir zone and hardness obtained through different process parameters. Arrows and dotted lines show cavities formation. SFZ: shoulder flow zone and NZ: nugget zone
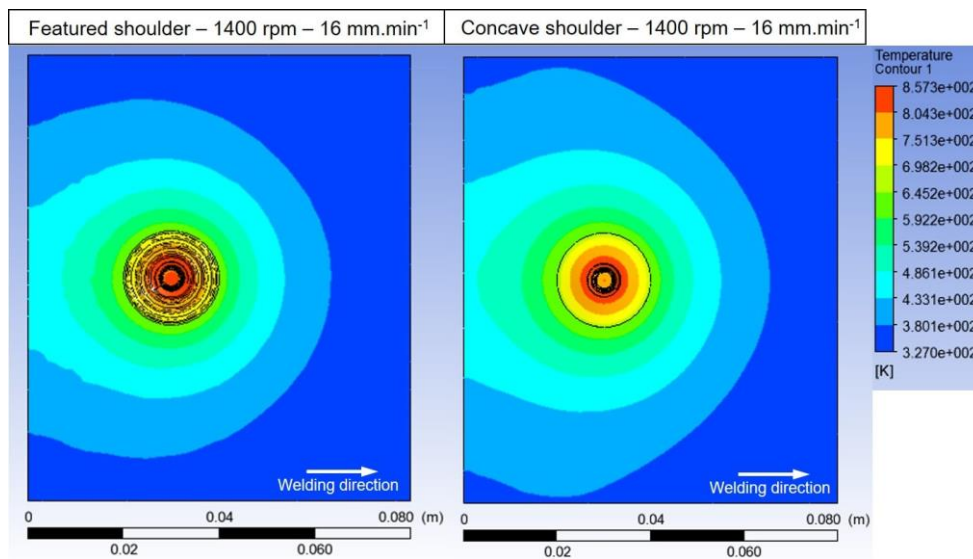

Figure 12. Modeling results of thermal distribution in welded section

There is a tendency to concentrate the heat at stir region when featured shoulder tools are used during FSW producing a greater amount of plasticizer heat. Under these conditions high cooling rates were produced, smallest grain size, and higher values of hardness at the stir region. Moreover, concave shoulder produces highest quantity of frictional heat more than plasticizer heat, which favours lower values of hardness at stir region. HAZ extension depends on the process parameters combination used. When R-values were higher, the width of HAZ also increased, being consistent with higher revolutions per unit of length producing a higher peak of temperature near to pin of tool [33]. In Figure 12 can be observed that the maximum peak of temperature was ~857 K in stir region. Width of HAZ is bigger for featured tools compared to concave tool. The extension of HAZ can be limited by statically recrystallization temperature since it experiences only a thermal cycle, which is in the range from 433 K to 486 K for aluminium alloys, Villegar et al., and McNelley et. al, in [33, 34].

Mechanical Properties of Welded Joints

Figure 13 shows the results of ultimate tensile strength (S_{ut}) and yield strength (S_y) of welded joints obtained using combinations of process parameters and different geometries' shoulder. All welded specimens showed lower Sut and Sy values than base material in as-received condition and they also fractured in the stir region. Table 6 shows that the highest tensile properties were reached using featured shoulder tool, allowing obtaining a 70 and 65% of joint efficiency with H-H and L-L parameters combinations, respectively. Although the above-mentioned tensile test results are lower than expected in base metal, these were higher than obtained results of similar welded joints in other works [13, 15].
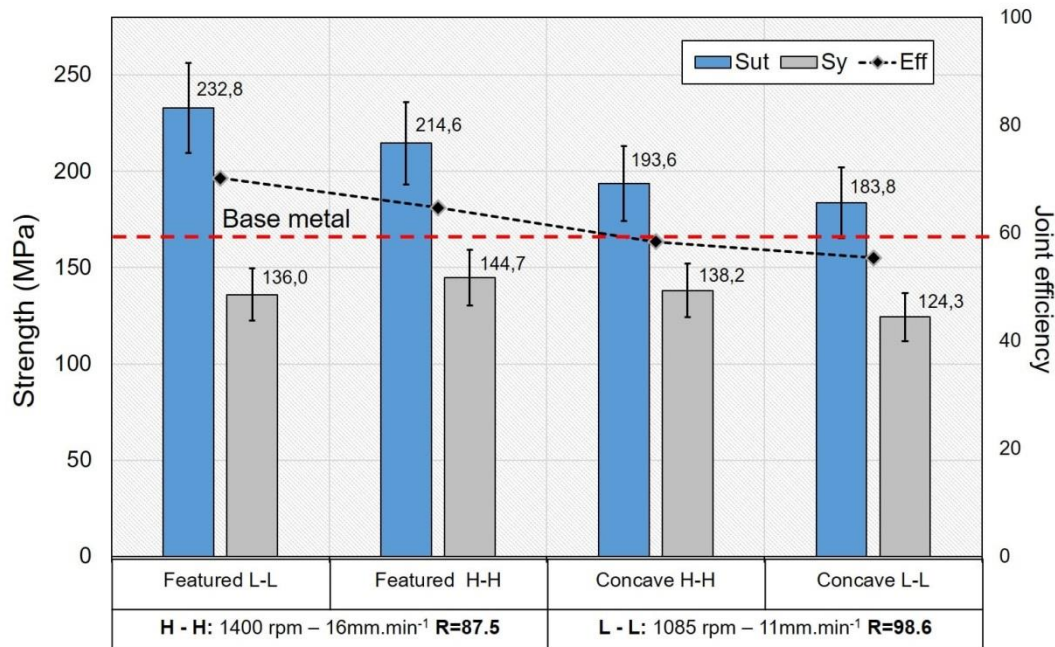

Figure 13. Tension test results of transverse section of welded joints

Failure locations of tensile test are coherent with cavities formation detected in stir region. That formation is caused probably because there was no force control during welding process in the milling machine used in this work. Surface fracture analysis of welded joints showed heterogeneities, according to location at regions of stir zone. Figure 14 shows that fracture surface of welded joints obtained using featured shoulder presents dimples at nugget zone (NZ), and a fibrously appearance on surface of failure at shoulder flow zone (SFZ). Meanwhile, for welded joints obtained using concave shoulder, it was observed a NZ notoriously more fibrous compared to those obtained using featured shoulder, additionally, failures matched with cavities formation region.

In the homogeneous zone NZ, a typical ductile failure was observed. Fractured surfaces have dimples with some precipitates inside the cavities. Since the interaction volume in the SEM is larger than the precipitates, it was not possible to conclude about the precise chemical composition of these precipitates by EDS measurements. However, it can be concluded that they are probably, α- and β- precipitates, as it was previously shown in Figure 8. SFZ zone is located aside the vertical split. The split is caused by the defects (cavities) observed in transverse section of joint and by the interface NZ / SFZ. Although, the fractured surfaces of Al-alloys are expected to be ductile (because of face centered cubic structure), in SFZ zone a brittle fracture was observed. This brittle fracture was detected since fibres detach from each other. The same fibres caused by a step of flow have been recently observed for FSW of aluminium by Sahu and Pal in [35].

Superimposition of hardness measurements profiles and calculated thermal distribution in cross section of welded joints are shown in Figure 15. The maximum hardness for the feature and concave L-L were observed in the stir region for both tools. A large revolution pitch (R) generated the widest HAZ. A high heat concentration near to the interface between stirred metal / tool was found when featured shoulder tools were used. Accordingly, the plasticizer heat produced the largest grain refinement in stir region resulting in the highest hardness. It can be noticed that for both cases of geometry of shoulder used, the HAZ extension is similar depending on R-value obtained. When the R-value is increased, the HAZ extension also increased, independently of process parameters combination. Simulation results showed that the peak temperature is 857 K at a region around the pin of the tool. That region was smaller when concave shoulder tool was used.
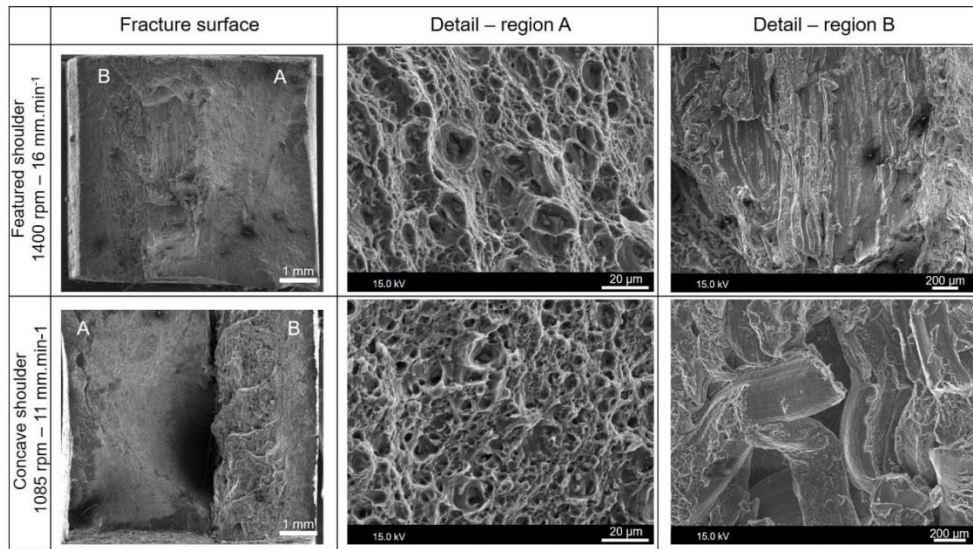
Figure 14. Fracture surface analysis of tensile test specimens. A: nugget zone. B: shoulder flow zone
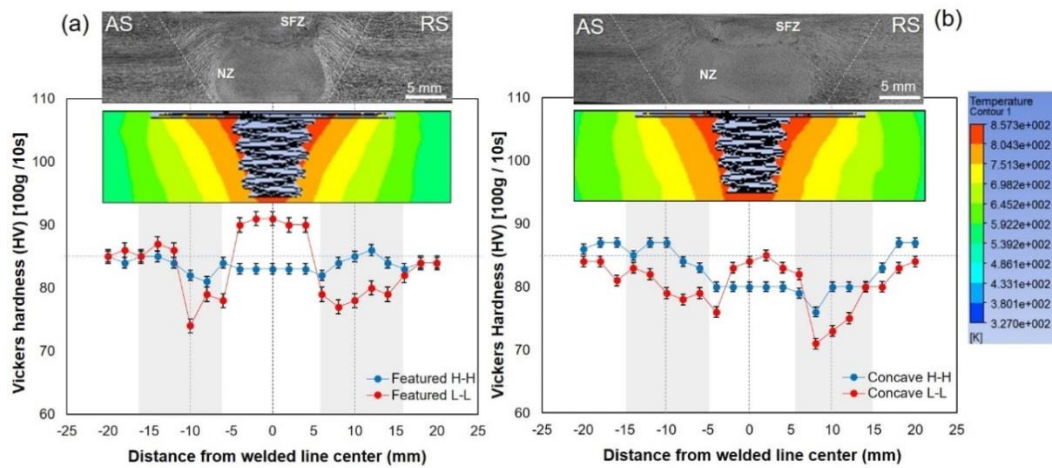

Figure 15. Superimposed graphical between microhardness profiles and thermal distribution results. (a) Featured shoulder, and (b) Concave shoulder. H-H: 1400 rpm – 16 mm.min^{-1} (R=87.5); L-L: 1085 rpm – 11 mm.min^{-1} (R=98.6)

Finally, the statistical results of experimental evaluation of combinations between process parameters and shoulder geometry of tool are shown in Figure 16. The evaluated factors were shoulder geometry of tool (F: featured, and C: concave shoulder, and they were numerically represented through surface area) and revolution pitch R-value, resulting in several combinations of process parameter as summarized in Table 6. The results of evaluation using an ANOVA analysis with fixed factors showed that increasing R-values produces statistically significant differences in ultimate strength (S_{ut}) values, particularly for high R-values and featured shoulder tool. This result is consistent with experimental values for strength and hardness obtained for L-L process parameters combinations.
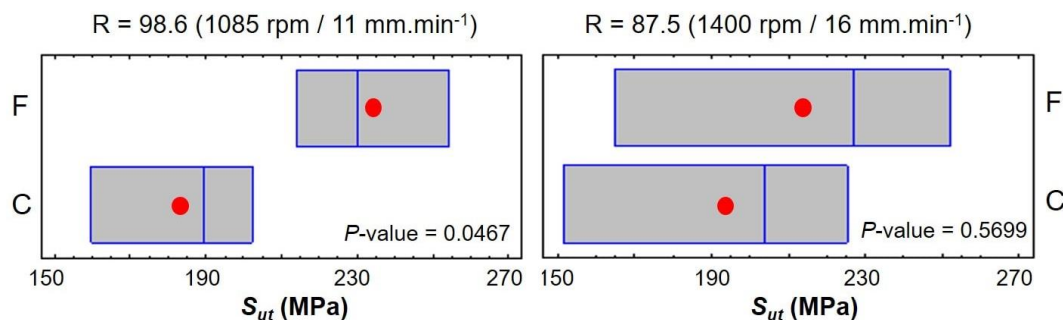

Figure 16. Box diagrams showing ANOVA analysis for process parameters and tool geometry combinations. F: Featured tool. C: Concave tool

Table 6. Summary of results of properties and characteristics of obtained welded joints

Shoulder geometry	Concave		Featured	
Parameters combination	H-H	L-L	H-H	L-L
R (rev.mm^{-1})	87.5	98.6	87.5	98.6
Maximum HV stir zone	80	83	84	90
S_{ut} (MPa)	193.6	183.8	214.6	232.8
S_y (MPa)	138.2	124.3	144.7	136.0
Width stir region (mm)	23	28.7	23.6	30.3
HAZ / TMAZ type	Extended	Extended	Concentrated	Concentrated

CONCLUSIONS

1. Feature and concave shoulder tools produced similar flow patterns in stir region. Two regions were observed named shoulder flow zone - SFZ at the top of stir zone and nugget zone - NZ at the bottom. These two zones were produced by material flux at pin and shoulder vicinities.

2. A correlation between mechanical properties and process parameters and geometry shoulder of tool combinations was established. High R-values increased the HAZ extension, producing high hardness in stir region, and grain size refinement.

3. Tools with featured shoulder concentrated the heat at a region near to pin of tool obtaining a narrow thermal distribution, unlike concave shoulder of tool, which showed a thermal distribution more extended with lower heat concentration. This fact was related to distribution of plasticizer heat and frictional heat associated to featured and plain/concave shoulders, respectively.

4. Cavities were observed in the boundary between shoulder flow zone and nugget zone. These defects affected tensile test results, obtaining S_{ut} and S_y lower than base metal. The highest resistance was found for welded joints obtained by featured shoulders.

5. The increase of R-values produced statistically significant differences in ultimate tensile strength (S_{ut}) values, particularly for higher R-values and featured shoulder of tools.

ACKNOWLEDGEMENTS

REFERENCES

[1] J. R. Davis, "ASM Specialty Handbook: Aluminum and Aluminum Alloys," *ASM Int.*, 1993.

[2] T. E. M. D. S. George, *Handbook of Aluminum Volume 1 Physical Metallurgy and Processes*. 1969.

[3] P. E. Philip A. Schweitzer, *METALLIC MATERIALS Physics, Mechanical and Corrosion Properties*. 2003.

[4] A. K. Vasudevan and R. D. Doherty, *Aluminum Alloys: Contemporary Research and Applications*. 1989.

[5] J. Zander and R. Sandström, "Modelling technological properties of commercial wrought aluminium alloys," *Materials & Design.*, 2009, doi: 10.1016/j.matdes.2009.02.004.

[6] E. Rastkerdar, M. Shamanian, and A. Saatchi, "Taguchi optimization of pulsed current GTA welding parameters for improved corrosion resistance of 5083 aluminum welds," *Journal of Materials Engineering and Performance.*, 2013, doi: 10.1007/s11665-012-0346-5.

[7] E. E. N. Nuñez, J. U. Silgado, J. E. T. Salcedo, and A. J. Ramírez, "Influence of gas mixtures Ar-He and Ar-He-O2 on weldability of aluminum alloy AA5083- O using automated GMAW-P," *Journal Soldagem & Inspeção*, 2014, doi: 10.1590/0104-9224/SI1903.06.

[8] P. L. Threadgilll, A. J. Leonard, H. R. Shercliff, and P. J. Withers, "Friction stir welding of aluminium alloys," *International Materials Reviews*, 2009, doi: 10.1179/174328009X411136.

[9] W. M. Thomas, E. D. Nicholas, J. C. Needham, M. G. Murch, P. Templesmith, and C. J. Dawes, "GB Patent application no. 9125978.8," 1991.

[10] R. Nandan, T. DebRoy, and H. K. D. H. Bhadeshia, "Recent advances in friction-stir welding - Process, weldment structure and properties," *Progress in Materials Science*. 2008, doi: 10.1016/j.pmatsci.2008.05.001.

[11] H. Bin Chen, K. Yan, T. Lin, S. Ben Chen, C. Y. Jiang, and Y. Zhao, "The investigation of typical welding defects for 5456 aluminum alloy friction stir welds," *Materials Science and Engineering: A*, 2006, doi: 10.1016/j.msea.2006.06.056.

[12] R. S. Mishra and Z. Y. Ma, "Friction stir welding and processing," *Materials Science and Engineering R: Reports*. 2005, doi: 10.1016/j.mser.2005.07.001.

[13] S. Amini, M. M. Nazari, and A. Rezaei, "Bending vibrational tool for friction stir welding process," *International Journal of Advanced Manufacturing Technology*, 2016, doi: 10.1007/s00170-015-7834-3.

[14] R. Kumar, K. Singh, and S. Pandey, "Process forces and heat input as function of process parameters in AA5083 friction stir welds," *Transactions of Nonferrous Metals Society of China (English Ed.*, 2012, doi: 10.1016/S1003-6326(11)61173-4.

[15] S. Jannet, P. K. Mathews, and R. Raja, "Optimization of process parameters of friction stir welded AA 5083-O aluminum alloy using Response Surface Methodology," *Bulletin of the Polish Academy of Sciences: Technical Sciences*, 2015, doi: 10.1515/bpasts-2015-0097.

[16] M. S. Han, S. J. Lee, J. C. Park, S. C. Ko, Y. Bin Woo, and S. J. Kim, "Optimum condition by mechanical characteristic evaluation in friction stir welding for 5083-O Al alloy," *Transactions of Nonferrous Metals Society of China (English Ed.*, 2009, doi: 10.1016/S1003-6326(10)60238-5.

[17] H. Taheri *et al.*, "Investigation of nondestructive testing methods for friction stirwelding," *Metals*. 2019, doi: 10.3390/met9060624.

[18] M. Imam *et al.*, "Deformation characteristics and microstructural evolution in friction stir welding of thick 5083 aluminum alloy," *International Journal of Advanced Manufacturing Technology*, 2018, doi: 10.1007/s00170-018-2521-9.

[19] T. Hirata *et al.*, "Influence of friction stir welding parameters on grain size and formability in 5083 aluminum alloy," *Materials Science and Engineering A*, 2007, doi: 10.1016/j.msea.2006.12.079.

[20] D. Klobčar, L. Kosec, A. Pietras, and A. Smolej, "Friction-stir welding of aluminium alloy 5083," *Materials Technology*, 2012.

[21] R. S. Thube, "Effect of Tool Pin Profile and Welding Parameters on Friction Stir Processing Zone, Tensile Properties and Micro-hardness of AA5083 Joints Produced by Friction Stir Welding," *International Journal of Engineering and Advanced Technology*, 2014.

[22] H. Fujii, L. Cui, M. Maeda, and K. Nogi, "Effect of tool shape on mechanical properties and microstructure of friction stir welded aluminum alloys," *Materials Science and Engineering: A*, 2006, doi: 10.1016/j.msea.2005.11.045.

[23] Z. W. Chen, T. Pasang, and Y. Qi, "Shear flow and formation of Nugget zone during friction stir welding of aluminium alloy 5083-O," *Materials Science and Engineering A*, 2008, doi: 10.1016/j.msea.2007.05.074.

[24] K. J. Colligan and R. S. Mishra, "A conceptual model for the process variables related to heat generation in friction stir welding of aluminum," *Scripta Materialia*, 2008, doi: 10.1016/j.scriptamat.2007.10.015.

[25] J. K. Paik, "Mechanical properties of friction stir welded aluminum alloys 5083 and 5383," *International Journal of Naval Architecture and Ocean Engineering*, 2009, doi: 10.3744/JNAOE.2009.1.1.039.

[26] D. Kim *et al.*, "Numerical simulation of friction stir butt welding process for AA5083-H18 sheets," *European Journal of Mechanics - A/Solids*, 2010, doi: 10.1016/j.euromechsol.2009.10.006.

[27] V. Joshi, K. Balasubramaniam, and R. V Prakash, "Study of Defects in Friction Stir Welded Aa 5083 By Radiography , Ultrasonic and Phased Array Ultrasonic Technique," *National Seminar & Exhibition on Non-Destructive Evaluation*, 2011.

[28] H. Lombard, D. G. Hattingh, A. Steuwer, and M. N. James, "Optimising FSW process parameters to minimise defects and maximise fatigue life in 5083-H321 aluminium alloy," *Engineering Fracture Mechanics.*, 2008, doi: 10.1016/j.engfracmech.2007.01.026.

[29] R. Leal and A. Loureiro, "Defects formation in friction stir welding of aluminium alloys," 2004, doi: 10.4028/www.scientific.net/msf.455-456.299.

[30] D. H. Choi, B. W. Ahn, D. J. Quesnel, and S. B. Jung, "Behavior of β phase (Al3Mg2) in AA 5083 during friction stir welding," *Intermetallics*, 2013, doi: 10.1016/j.intermet.2012.12.004.

[31] R. Goswami, G. Spanos, P. S. Pao, and R. L. Holtz, "Precipitation behavior of the β phase in Al-5083," *Materials Science and Engineering: A* 2010, doi: 10.1016/j.msea.2009.10.007.

[32] J. Unfried-Silgado, A. Torres-Ardila, J. C. Carrasco-García, and J. Rodríguez-Fernández, "Effects of shoulder geometry of tool on microstructure and mechanical properties of friction stir welded joints of AA1100 aluminum alloy," *DYNA*, vol. 84, no. 200, 2017, doi: 10.15446/dyna.v84n200.55787.

[33] J. F. Villegas, A. M. Guarín, and J. Unfried-Silgado, "A Coupled Rigid-viscoplastic Numerical Modeling for Evaluating Effects of Shoulder Geometry on Friction Stir-welded Aluminum Alloys," *International Journal of Engineering, Transactions B: Applications* 2019, doi: 10.5829/ije.2019.32.02b.17.

[34] T. R. McNelley, S. Swaminathan, and J. Q. Su, "Recrystallization mechanisms during friction stir welding/processing of aluminum alloys," *Scripta Materialia*, 2008, doi: 10.1016/j.scriptamat.2007.09.064.

[35] P. K. Sahu and S. Pal, "Mechanical properties of dissimilar thickness aluminium alloy weld by single/double pass FSW," *Journal of Materials Processing Technology.*, 2017, doi: 10.1016/j.jmatprotec.2017.01.009.